ACS APPLIED MATERIALS & INTERFACES

Research Article

www.acsami.org

Effects of Interface States on Photoexcited Carriers in ZnO/Zn_2SnO_4 Type-II Radial Heterostructure Nanowires

Baochang Cheng,*[,†,‡] Guohong Wu,[†] Zhiyong Ouyang,[†] Xiaohui Su,[‡] Yanhe Xiao,[†] and Shuijin Lei[†]

[†]School of Materials Science and Engineering and [‡]Nanoscale Science and Technology Laboratory, Institute for Advanced Study, Nanchang University, Jiangxi 330031, P. R. China

ABSTRACT: Type-II band alignment of heterostructure contributes to spatially separate electrons and holes leading to an increase in minority carrier lifetime, which has much more advantages in photocatalytic activities and photovoltaic device applications. Here, Zn_2SnO_4-sheathed ZnO radial heterostructure nanowires were constructed to investigate systematically interfacial charge separation. The lattice mismatch between ZnO and Zn_2SnO_4 induces interface states to exist at their heterointerface. At low pump fluence, photoexcited charges are localized within the ZnO core rather than separated due to the large interface barrier. Correspondingly, only ZnO-related bandedge ultraviolet (UV) and green emissions are dominated in photoluminescence spectra. At high pump fluence, however, impurities are ionized and electrons trapped in interface states are excited, resulting in a decrease in interface barrier, which makes photogenerated charges efficiently separated at their heterointerface by direct tunneling, and, consequently, an additional blue-violet emission, attributed to the heterointerface recombination of electrons in Zn_2SnO_4 conduction band (CB) and holes in ZnO valence band. Additionally, the heterointerface can separate effectively photoexcited carriers and form a photovoltaic effect. Our results provide the localization/separation condition of photogenerated charges for the type-II band alignment of core/shell heterostructure, which should be very useful for the realization of underpinned mechanism of the developed optoelectronic devices.

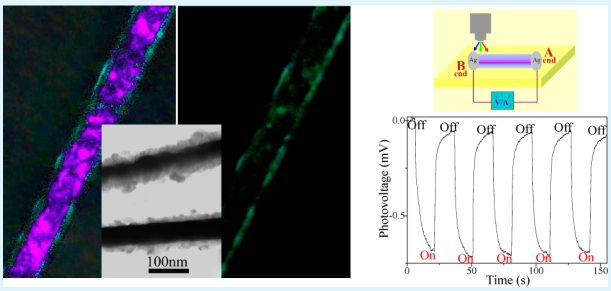

KEYWORDS: *ZnO, Zn_2SnO_4, core/shell nanowires, radial heterostructure, exciton localization and separation, interface states*

1. INTRODUCTION

Semiconductor nanowires (NWs) are attracting a strongly increasing interest since they can be served as building blocks for nanometer-scale electronic and optoelectronic devices including field effect transistors,[1] light emitting diodes,[2] photodetectors,[3] gas sensors,[4] and solar cells.[5] Due to the remarkable surface-to-volume ratio, surface states play very important roles in the physical properties of NWs. In particular, Fermi level pinning at surface states is expected which would result in band bending and depleted regions in the vicinity of surfaces and/or interfaces.[6,7] In order to meet the ever-increasing demand in device performance, it is need to tailor the properties of semiconductors which can be done by design and controlled fabrication of new nanostructures. For example, wide bandgap semiconductors were constructed into core/shell heterostructure systems.[8−11] As is well-known, it is generally accepted that electrons and holes are both confined within the core for type I band alignment, which make it advantageous in photoluminescence (PL). For type II band alignment, however, both the valence band maximum and the conduction band minimum in one semiconductor are lower in energy than their counterparts in the second semiconductor. This band alignment contributes to spatially separate electrons and holes leading to an increase in minority carrier lifetime, which make it advantageous in photocatalytic activities and photovoltaic device applications.[12−14] In general, it is difficult for the lattices composed of heterostructures to match exactly. At the heterointerface, hence, strains can induce quantities of interface states, which would play a key role in its physical properties. For type II core/shell heterostructures, interestingly, high luminescence quantum yields can also be determined when exciting the core.[15,16]

Due to a wide direct bandgap of 3.37 eV and a large exciton binding energy of 60 meV, ZnO nanostructures have been recognized as promising candidates to realize short wavelength exciton-related devices such as ultraviolet (UV) emitters and lasers.[16,17] Generally speaking, the room temperature emission from ZnO NWs always demonstrates a weak near-band-edge (NBE) emission in the UV region and a broad deep level emission (DLE) in the green region.[18] Besides the two emissions, blue, yellow, and red emissions can also be observed sometimes in the visible spectral region, which are generally attributed to defect emissions simply.[19] Especially for the green emission, its assignment is highly controversial.[20] Ternary oxide Zn_2SnO_4 is also an important n-type semiconductor material with a bandgap energy of 3.6 eV,[21,22] which has promising applications in photovoltaic devices,[23−28] photocatalysts to decompose organic wastes,[29] humidity detection,[30,31] Li^+

Received: December 4, 2013
Accepted: February 21, 2014
Published: February 21, 2014

 © 2014 American Chemical Society dx.doi.org/10.1021/am405569k | ACS Appl. Mater. Interfaces 2014, 6, 4057−4062

batteries,[32] and transparent conducting substrate due to its high electron mobility, high electrical conductivity, and high transmittance.[33,34] Moreover, its conduction band (CB) edge energy is lower than that of ZnO. When it couples with ZnO, therefore, type II band alignment would be expected to be formed at their interfaces. To gain a better understanding of electron localization/separation present in the type II heterostrucure NWs, here, we construct Zn_2SnO_4-sheathed ZnO core/shell heterostructure NWs and then present the observation of unusual properties in the PL of as-grown nanostructured ensembles excited by a He−Cd laser with a wavelength of 325 nm under different power densities. We provide the direct evidence of the optical transition arising from type II band alignment in heterostructure nanorods based on the interfacial state filling and band bending near the interface. The blue-violet and green emissions are well-identified as the heterointerface emission and the recombination of electrons in CB and trapped holes and/or V_O^{**} located in interface depletion layer. Interestingly, the magnitude of the red-shift of type II band alignment transition increases as increasing excitation pumping power, which gives us a firm evidence to support our interpretation. In addition, the visualized PL image experiment of an individual NW also confirms our proposed band alignment. We show that this phenomenon is governed by a pure interface effect, namely, a filling and creating of interface states.

2. EXPERIMENTAL METHODS

2.1. Preparation of ZnO/Zn_2SnO_4 Core/Shell Radial Heterostructure NWs. The ZnO/Zn_2SnO_4 NWs used for this study were synthesized by a polymeric sol−gel method followed by a postannealing. $Zn(NO_3)_2{\cdot}6H_2O$, $SnCl_2{\cdot}2H_2O$, citric acid, and ethylene glycol were added to deionized water at a molar ratio of 5:1:5:30. A sol was formed at 80 °C and, subsequently, polymerized to a gel at 150 °C. The solid gel was prepyrolyzed at 400 °C to form an amorphous composite precursor. The resulting precursor was ground, placed in a ceramic crucible covered with a ceramic lid, and then put into a box furnace and heated at 1000 °C for 120 min.

2.2. Characterization and Optical Measurement of Materials. The morphology, and microstructures of as-synthesized NWs were characterized by X-ray diffraction (XRD, RIGAKU D/max-3b), field-emission scanning electron microscopy (FE-SEM, FEI Quanta 200F), high-resolution transmission electron microscopy (HRTEM, JEOL 2010), and selected-area electron diffraction (SAED), respectively. The excitation density dependence of PL spectra were performed by the micro-PL system of a confocal laser micro-Raman spectrometer (LABRAM-HR, France JY Company) using the 325 nm line of a He−Cd laser with an output power of about 5 mW as a excitation sources and the incident light is focused on a spot of about 5 um diameter by a microscopic objective. For the PL mapping experiments, NWs were dispersed on a thin quartz substrate and then observed by a laser scanning confocal microscopy (LSCM, Zeiss LSM710) using a diode laser with a wavelength of 405 nm as an excitation source. The light emitted from the core/shell heterostructures was collected by an objective lens. The detection system operates efficiently in the spectral range from 420 to 720 nm. For the photovoltaic experiment, the microbeam excitation light was given out by a microscope objective and the electric measurements were carried out by low-noise preamplifier (Stanford Research System Model SR560) and low-noise current preamplifier (Stanford Research System Model SR570).

3. RESULTS AND DISCUSSION

The XRD pattern of as-synthesized nanostructure is shown in Figure 1a. Diamond-cubic Zn_2SnO_4 (JCPDS file: 24-1470) and

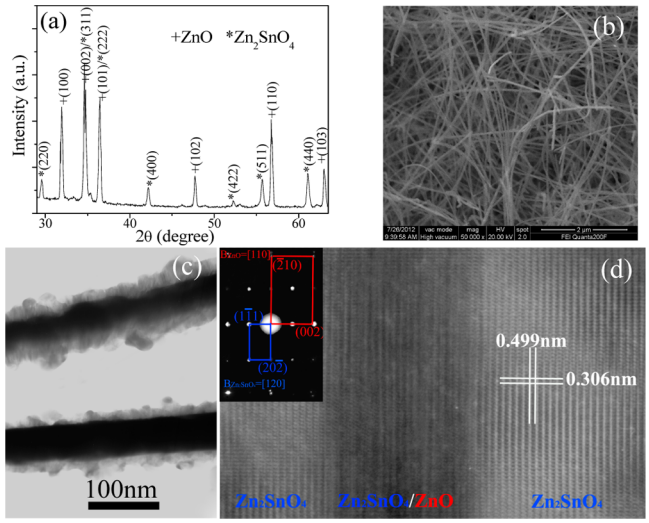

Figure 1. Structural characterization of ZnO/Zn_2SnO_4 core/shell heterostructure NWs. (a) A representative XRD pattern from a collection of nanostructures; (b) FE-SEM image; (c) TEM images showing the core/shell heterostructures with dark core and bright shell; (d) HRTEM image, taken from the core/shell heterointerface area, (inset) Corresponding SAED pattern, showing a superposition of two specific patterns, which can be indexed to a hexagonal structured ZnO with [110] zone axis and an orthorhombic structured Zn_2SnO_4 with [120] zone axis.

wurtzite-hexagonal ZnO (JCPDS file: 36-1451) are obviously observed, indicating that the product is composed of Zn_2SnO_4 and ZnO. Figure 1b shows a typical distribution in the morphology for nanostructures by FE-SEM. The image reveals that NWs are predominant in the sample, varying in length from several to several tens of micrometers. As seen from a bright-field image of TEM (Figure 1c), the product presents a wire-like morphology. Moreover, there is a great difference in contrast between core and shell, showing "dark" core and "bright" shell along the axis of the NWs with relatively sharp interfaces. It indicates that the structure of the edges is different from that of the core, which means the NWs with a core/shell coaxial heterostructure are synthesized successfully. The selected area electron diffraction (SAED) pattern (Figure 1d) indicates a superposition of two sets of single-crystal diffraction spots, which can be indexed to the [110] zone axis ZnO and the [120] zone axis Zn_2SnO_4 with an epitaxial relationship of $(001)_{ZnO}\|(1\bar{1}1)_{Zn_2SnO_4}$, $(\bar{2}10)_{ZnO}\|(20\bar{2})_{Zn_2SnO_4}$, and $[120]_{ZnO}\|[121]_{Zn_2SnO_4}$. The lattice mismatch is about −10% between $(001)_{ZnO}$ and $(1\bar{1}1)_{Zn_2SnO_4}$, and −6.2% between $(\bar{2}10)_{ZnO}$ and $(40\bar{4})_{Zn_2SnO_4}$ (in reference to ZnO). The lattice mismatch, therfore, exerts some stress on their heterointerface. Figure 1d is a high-resolution TEM image, taken from the heterointerface region of an individual ZnO/Zn_2SnO_4 NW. Due to the coating of Zn_2SnO_4 on the surface of ZnO core, atom resolution image of Zn_2SnO_4 from the outer shell can be observed clearly, while the image of ZnO core cannot be

observed obviously. Because Zn content is higher than Sn in our experiment, the excess Zn can form ZnO. For the synthesis method of a polymeric sol–gel followed by a postannealing, ZnO can be formed about 850 °C.[35] For the growth of SnO_2 by his method, however, it needs a higher temperature of about 1100 °C.[36] Therefore, ZnO may grow first. Subsequently, Sn was reduced by carbon at higher temperature, and coating on the ZnO surface. Tin oxides can react with ZnO and form Zn_2SnO_4. Since the tin content is not sufficient, Zn_2SnO_4-seathed ZnO core/shell nanowires can be formed eventually.

The optical properties of ZnO/Zn_2SnO_4 core/shell heterostructure NWs were investigated by PL. Figure 2a–d shows the pumping power dependence of the PL spectra measured at room temperature. At relatively low excitation power density of $0.1I_0$, the PL spectra are composed of a strong UV peak at around 381 nm, related to the near-band-edge (NBE) emission of ZnO, and a broad visible emission band centering at 525 nm. The position of the NBE emission peak exhibits a redshift, and however, its intensity decreases first and then increases gradually with increasing excitation intensity. The broad visible emission band completely quenches at higher excitation intensity. Quite interestingly, it is found that a new emission peak appears at the low-energy side of the NBE emission. With increasing excitation intensity, not only its intensity increases but its position shows a much larger redshift. Moreover, the interval between the two UV peaks increases with increasing excitation density.

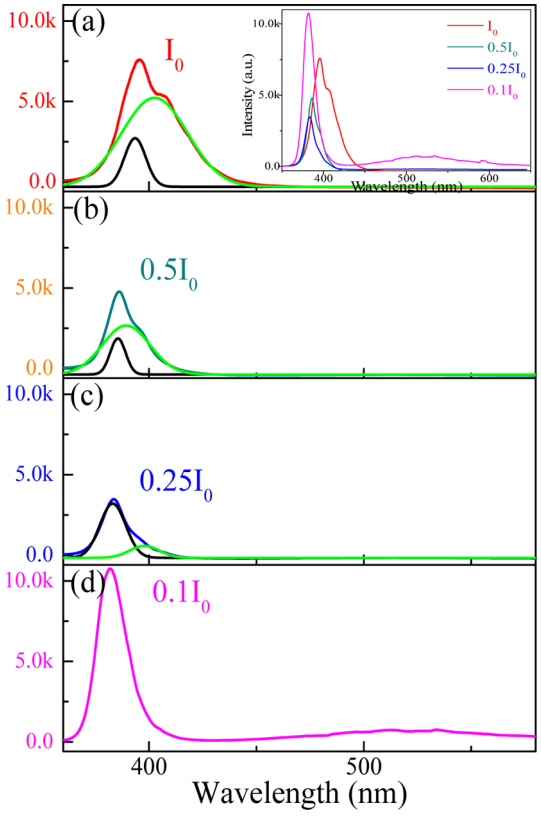

Figure 2. (a–d) Excitation density dependent PL spectra, I_0 about 20 kW/cm^2. The black and green solid curves correspond to the multipeak fit for the UV emission and represent respectively NBE and heterointerface emissions. (a inset) Pattern in which all PL spectra are integrated.

For ZnO and Zn_2SnO_4, their lattices mismatch based on the above HRTEM analysis, and moreover, they are both n-type semiconductors with wide bandgap. Therefore, quantities of acceptor-type surface/interface states can form at their heterointerface. Under the thermal equilibrium state or relatively low excitation intensity, internal electrons will diffuse toward the interface states, resulting into an upward bending for both CB and valence band (VB), that is, a low conductive depletion layer is formed near the heterointerface. Particularly, the high concentration of interface states can induce Fermi level pinning, and the corresponding band diagram is shown in Figure 3a. The relatively large interface barrier prevents charges from separating. Therefore, photogenerated electron–hole pairs are completely localized within ZnO at relatively low excitation power density. As a consequence, only ZnO-related UV emission peak and broad visible emission band are observed in PL spectra, respectively arising from the exciton annihilation and the recombination of electrons in CB and trapped holes and/or oxygen vacancies (V_O^{**}) located in the depletion region.

At low excitation intensity, the nonequilibrium carrier density is much lower than the doping concentration. However, as the sample is illuminated by UV light at relatively high power density, impurities will be ionized and, moreover, trapped electrons will also be excited and then released from original interface states. Thus, quantities of electrons were generated, namely, an increase in effective density of electrons, resulting into an unpinning of Fermi level. Consequently, the energy band moves downward, and correspondingly, the height and width of the interface barrier both decrease. The effective barrier height ϕ_{eff} is related to the depletion layer width (λ) on the two sides of the interface as[37−39]

$$\lambda = \left[\frac{2\varepsilon\phi_{eff}}{eN_d}\right]^{1/2} \quad (1)$$

where e is the electronic charge, N_d is the doping density, and ε is the dielectric constant of ZnO or Zn_2SnO_4. The change in λ (change in channel area) in relation with ϕ_{eff}.

Near the heterointerface, the energy band of ZnO and Zn_2SnO_4 gradually moves downward with increasing excitation power intensity. When the λ is lower than the mean free path of electrons, it will be very easy for electrons to cross the interface barrier by direct tunneling (see Figure 3b). Thus, the downward bending of the energy band at the ZnO/Zn_2SnO_4 heterointerface can cause the spatial separation of photoexcited carriers. Additionally, the electron affinity of Zn_2SnO_4 is lower than that of ZnO, and consequently, electrons flux to Zn_2SnO_4 while holes flux to ZnO. Hence, electrons are accumulated in the surface region of Zn_2SnO_4 while holes are accumulated in the surface region of ZnO. With further increasing excitation intensity, the band-bending effect becomes more pronounced, and the accumulated photoexcited carriers will be confined in a narrower region in the vicinity of the interface. Thus, an increase in excitation density raises the steepness of the confining potential, and consequently, the quantization energy is enhanced, resulting in an appearance of interface transition and moreover a spectral redshift.

Due to ionization of impurities and excitation of electrons trapped in interface states at high excitation intensity,[40] the effective density of electrons increases, resulting into a rise in Fermi level. With further increasing pump fluence, the Fermi level will exceed to CB edge energy, and thus, ZnO and

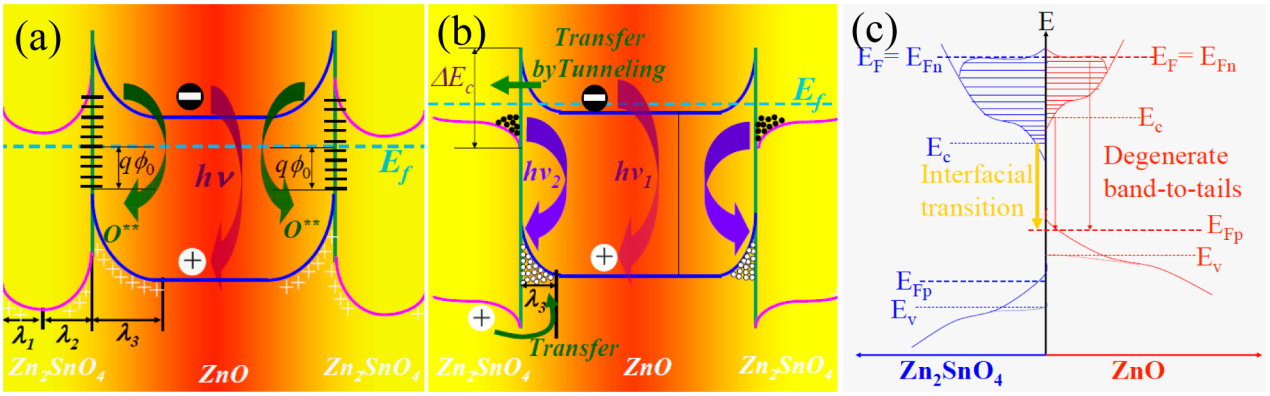

Figure 3. Band diagrams of type II alignment of Zn_2SnO_4/ZnO heterostructure NWs. (a) At low excitation intensity, interface states makes photogenerated charges confined within ZnO core, and the ZnO-related bandedge exciton annihilation and the recombination of electrons in CB and holes in the interface depletion region is dominated. (b) At high excitation intensity, the elimination of interfacial barrier results into an efficient separation of photogenerated charges by direct tunneling at the heterointerface, and the emission mainly arises from the heterointerface recombination of electrons accumulated near Zn_2SnO_4 and holes accumulated near ZnO and accompanied simultaneously weak bandedge exciton annihilation. (c) The schematic drawing of optical transition from degenerate CB of ZnO and Zn_2SnO_4 to VB tailing states of ZnO.

Zn_2SnO_4 can form degenerate semiconductors. Additionally, the increase in excitation intensity also results in the dissociation of excitons to electron–hole plasma (EHP) (Mott transition). The strong Coulomb interaction among electrons and holes in the EHP induces many body effects, which leads to bandgap renormalization (BGR) accompanied by consequent redshift of the NBE emission.[41−43] At high excitation intensity, therefore, the NBE emission is typically characteristic for "free-to-bound" radiative recombination of degenerate electrons in the CB and nonequilibrium holes located in the VB tails [see Figure 3c] The shape of the emission bands in these spectra closely reproduces the energy distribution of electrons in the CB, while their energy positions are determined by the interplay between the equilibrium Burstein–Moss shift and the effective bandgap renormalization. PL peak energy can then be expressed as

$$E = E_c(k) - \Delta E_{e-e} - \Delta E_{e-i} - E_T^* \quad (2)$$

where $E_c(k)$ represents the nonparabolic CB dispersion relation, ΔE_{e-e} and ΔE_{e-i} are the terms originated from electron–electron and electron–ionized impurity interactions as results of many body effects, and E_T^* is the potential minima of the valence band tails near the thermal-equilibrium level.

Since the bandgap of Zn_2SnO_4 is broader than that of ZnO, the emission of Zn_2SnO_4 can be reabsorbed both by ZnO and their interface, leading to a disappearance of Zn_2SnO_4 emission. For the broad green emission of ZnO, despite the extensive studies over the past few decades, its origin has not yet been identified. Proposed origins include: (i) extrinsic Cu impurities,[44] (ii) surface-related states,[45] and (iii) intrinsic defects such as oxygen vacancy (V_O),[46,47] zinc vacancy (V_{Zn}),[48] oxygen antisite (O_{Zn}),[49] and Zn interstitial (Zn_i),[50,51] or their complexes.[52] Generally, it is believed to originate from deep level defects-related emission, for instance, oxygen-vacancy.[46] For type II ZnO/Zn_2SnO_4 heterostructure, in the symmetric state, the width of interface depletion region is relatively large due to surface state pinning. Moreover, majority carriers (electrons) are almost depleted in depletion region, where positive charged V_O^{**} and trapped holes can exist. At high excitation intensity, however, the increase of free-electron concentration results into a decrease in depletion layer width. Therefore, the broad visible emission should associate with the surface depletion layer of ZnO NWs. Thus, the green emission band should be attributed to the recombination of electrons in CB and/or shallow donor levels and V_O^{**} and trapped holes located in interface depletion layer.

To gain more insight into the emission mechanism of ZnO/Zn_2SnO_4, we have selected an individual heterostructure with a relatively large diameter and then performed the direct observation for its emission using a LSCM, as shown in Figure 4a and b. The applied laser wavelength is 405 nm, which is lower than both the energy gaps of ZnO and Zn_2SnO_4. From the fluorescent image, it can be seen that the green emission only appears in the surface layer, while the blue–violet emission seemingly exists in the core. However, the distribution of the blue–violet emission is quite uneven, which should originate from the structure and composition fluctuations at the heterointerface, and hence, it should be more reasonable to ascribe the blue–violet emission to the core/shell heterointerface emission. It is due to the separation and transfer of photoexcited charges that results into a recombination of electrons in Zn_2SnO_4 CB and holes in ZnO VB at the type-II heterointerface.

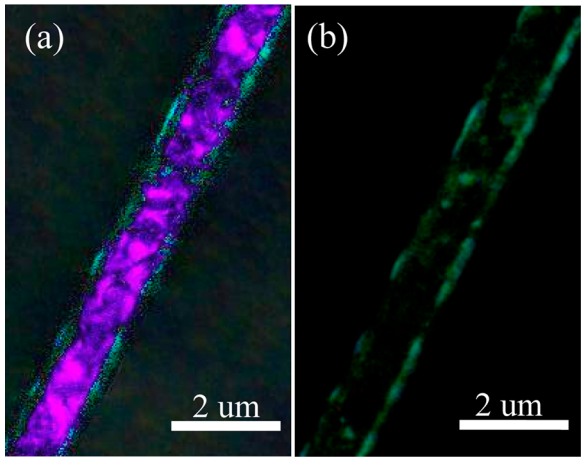

Figure 4. (a) Original fluorescent image of an individual ZnO/Zn_2SnO_4 heterostructure measured by LSCM. (b) Fluorescent image in which blue–violet light was removed.

dx.doi.org/10.1021/am405569k | ACS Appl. Mater. Interfaces 2014, 6, 4057−4062

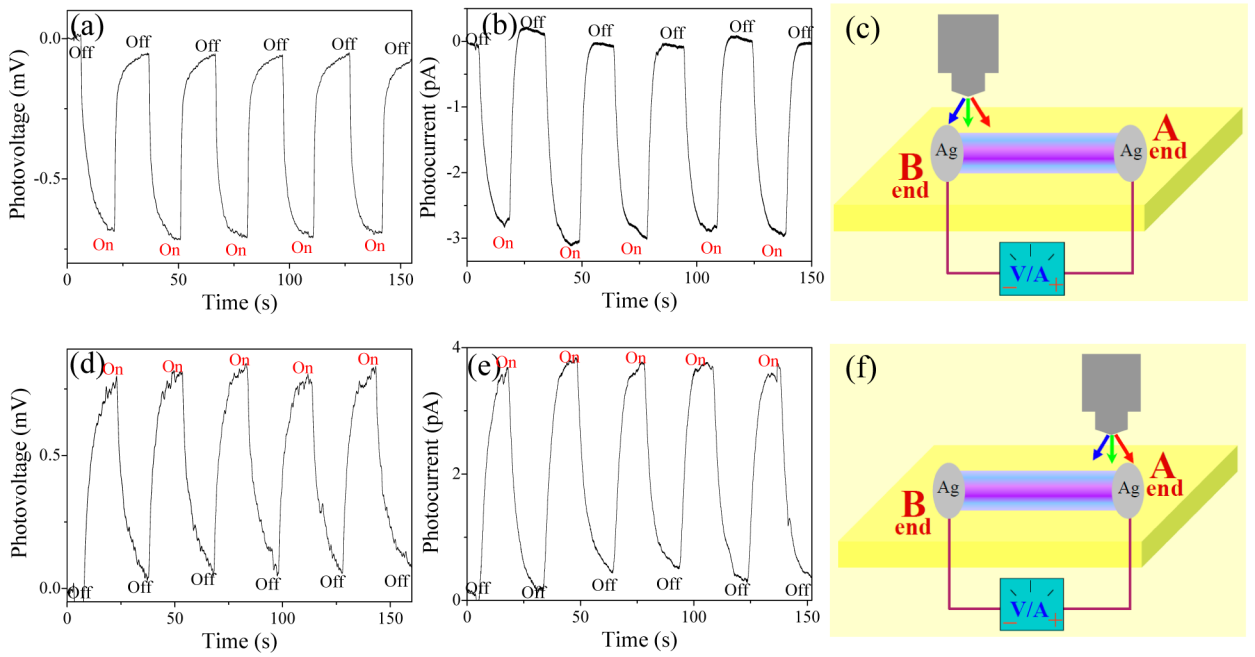

Figure 5. At zero bias voltage, the output signal of photovoltage and photocurrent under alternating light on and light off. (a and b) End connected to the cathode of voltmeter and ammeter is illuminated by a microbeam visible light. (c) Schematic diagram of photovoltaic testing device. (d and e) End connected to the anode of voltmeter and ammeter is illuminated by a microbeam visible light. (f) Schematic diagram of photovoltaic testing device.

In order to understand the separation and transfer properties of photogenerated charges at the ZnO/Zn_2SnO_4 heterointerface in more details, we have performed the photovoltaic experiments, as shown in Figure 5. At zero bias, one end of the $Ag-ZnO/Zn_2SnO_4-Ag$ device is illuminated with a microbeam light from an optical microscopy objective. It can be seen that the device, based on an individual heterostructure NW, shows obvious photovoltage of ~0.8 mV and photocurrent of ~3.5 pA between the two electrodes at both ends, and moreover, the potential of the end subjected to the light illumination is positive while that of the other is negative. Additionally, the photoresponse is prompt, steady, and reproducible during repeated on/off cycles of the visible light illumination. This result further confirms that the photogenerated carriers can be separated effectively and then electrons migrate to Zn_2SnO_4 shell upon the light illumination. Subsequently, the electrons, accumulated in the Zn_2SnO_4 shell, can freely diffuse toward the other end along Zn_2SnO_4 shell layer, resulting in a negative potential at the end without illumination. After illuminating the reverse end of the device to the measurement system, the opposite signals were observed, suggesting that the measured signals were generated by the device. These results demonstrate the as-prepared nanostructured radial heterojunction can effectively harvest light and yield an obvious photovoltaic effect.

4. CONCLUSIONS

In summary, we have provided the direct experimental probe of the optional transition for Zn_2SnO_4-sheathed ZnO heterostructure NWs by different pump fluences and visualized observation using LSCM. At low excitation density, the presence of interface states, arising from the lattice mismatch at ZnO/Zn_2SnO_4 heterointerface, results into the pinning of Fermi energy level. Due to relatively large interface potential barrier, therefore, photogenerated charges are localized within ZnO core rather than separated efficiently at the heterointerface. As a consequence, only the ZnO-related UV and visible emissions, respectively corresponding to the exciton annihilation and the recombination of electrons in CB and trapped holes and/or V_O^{**} in surface depletion layer, are dominant. At high excitation density, however, impurities are ionized and trapped electrons in interface states are excited, resulting into a decrease in interface potential barrier. As the width of depletion region is lower than mean free path of electrons, photogenerated charges can be efficiently separated and transferred by direct tunneling at the heterostructure interface, and consequently, electrons migrate to Zn_2SnO_4 while holes migrate to ZnO. As a result, the heterointerface emission, arising from the recombination of electrons accumulated in Zn_2SnO_4 CB and holes accumulated in ZnO VB, can be observed obviously. The photovoltaic experiments show that the radial heterostructure can effectively separate photogenerated carriers and yield an obvious photovoltaic effect. Additionally, high pump fluence also induces bandgap renormalization accompanied by consequent redshift of bandgap emission. For type-II band alignment of core/shell heterostructures, it will benefit the localization of photogenerated electron–hole pairs within the core with a low energy gap at relatively low excitation intensity, correspondingly increasing its luminescence quantum yields. At high excitation intensity, however, it will have advantages in photocatalytic activities and photovoltaic device applications due to efficient separation and transfer of charges. The establishment of the type-II band alignment should prove to be an effective route for the understanding and application of optoelectronic device derived from heterostructures.

AUTHOR INFORMATION

Corresponding Author

*E-mail: bcheng@vip.sina.com. Fax: +86-791-8396-9329.

Notes

The authors declare no competing financial interest.

■ ACKNOWLEDGMENTS

This work was supported by the Natural Science Foundation of China (51162023, 21263013), the Project for Young Scientist Training of Jiangxi Province (20133BCB23002), the Natural Science Foundation of Jiangxi Province (20132BAB206005, 20114BAB206027), and the Foundation of Jiangxi Educational Committee (GJJ13058). Y.X. and S.L. thank the Natural Science Foundation of China (51002073, 21001062) for support.

■ REFERENCES

(1) Ju, S.; Lee, K.; Janes, D. B.; Yoon, M. H.; Facchetti, A.; Marks, T. J. *Nano Lett.* **2005**, *5*, 2281−2285.
(2) Nadarajah, A.; Word, R. C.; Meiss, J.; Könenkamp, R. *Nano Lett.* **2008**, *8*, 534−537.
(3) Kind, H.; Yan, H.; Messer, B.; Law, M.; Yang, P. *Adv. Mater.* **2002**, *14*, 158−160.
(4) Zhang, Y.; Xu, J.; Xiang, Q.; Li, H.; Pan, Q.; Xu, P. *J. Phys. Chem. C* **2009**, *113*, 3430−3435.
(5) Law, M.; Greene, L. E.; Johnson, J. C.; Saykally, R.; Yang, P. *Nat. Mater.* **2005**, *4*, 455−459.
(6) Jones, F.; Léonard, F.; Talin, A. A.; Bell, N. S. *J. Appl. Phys.* **2007**, *102*, 014305.
(7) Liao, Z. M.; Liu, K. J.; Zhang, J. M.; Xu, J.; Yu, D. P. *Phys. Lett. A* **2007**, *367*, 207−210.
(8) Cheng, B. C.; Ouyang, Z. Y.; Chen, C.; Xiao, Y. H.; Lei, S. J. *Sci. Rep.* **2013**, *3*, 3249.
(9) Kundu, P.; Deshpande, P. A.; Madras, G.; Ravishankar, N. *J. Mater. Chem.* **2011**, *21*, 4209−4216.
(10) Hao, Y. F.; Meng, G. W.; Wang, Z. L.; Ye, C. H.; Zhang, L. D. *Nano Lett.* **2006**, *6*, 1650−1655.
(11) Hao, Y. F.; Meng, G. W.; Ye, C. H.; Zhang, L. D. *Appl. Phys. Lett.* **2005**, *87*, 033106.
(12) Pan, K.; Dong, Y.; Zhou, W.; Pan, Q.; Xie, Y.; Xie, T.; Tian, G.; Wang, G. *ACS Appl. Mater. Interfaces* **2013**, *5*, 8314−8320.
(13) Rakshit, T.; Mondal, S. P.; Manna, I.; Ray, S. K. *ACS Appl. Mater. Interfaces* **2012**, *4*, 6085−6095.
(14) Talapin, D. V.; Nelson, J. H.; Shevchenko, E. V.; Aloni, S.; Sadtler, B.; Alivisatos, A. P. *Nano Lett.* **2007**, *7*, 2951−2959.
(15) Carbone, L.; Nobile, C.; De Giorgi, M.; Sala, F. D.; Morello, G.; Pompa, P.; Hytch, M.; Snoeck, E.; Fiore, A.; Franchini, I. R.; Nadasan, M.; Silvestre, A. F.; Chiodo, L.; Kudera, S.; Cingolani, R.; Krahne, R.; Manna, L. *Nano Lett.* **2007**, *7*, 2942−2950.
(16) Tang, Z. K.; Wong, G. K. L.; Yu, P.; Kawasaki, M.; Ohtomo, A.; Koinuma, H.; Segawa, Y. *Appl. Phys. Lett.* **1998**, *72*, 3270−3272.
(17) Zhang, B. P.; Binh, N. T.; Wakatsuki, K.; Segawa, Y.; Yamada, Y.; Usami, N.; Kawasaki, M.; Koinuma, H. *Appl. Phys. Lett.* **2004**, *84*, 4098−4100.
(18) Zeng, H.; Duan, G.; Li, Y.; Yang, S.; Xu, X.; Cai, W. *Adv. Funct. Mater.* **2010**, *20*, 561−572.
(19) Djurišić, A. B.; Leung, Y. H. *Small* **2006**, *2*, 944−961.
(20) Li, M. J.; Xing, G. C.; Xing, G. Z.; Wu, B.; Wu, T.; Zhang, X. H.; Sum, T. C. *Phys. Rev. B* **2013**, *87*, 115309.
(21) Coutts, T. J.; Young, D. L.; Li, X.; Mulligan, W. P.; Wu, X. *J. Vac. Sci. Technol. A* **2000**, *18*, 2646−2660.
(22) Alpuche-Aviles, M. A.; Wu, Y. *J. Am. Chem. Soc.* **2009**, *131*, 3216−3224.
(23) Tan, B.; Toman, E.; Li, Y. G.; Wu, Y. Y. *J. Am. Chem. Soc.* **2007**, *129*, 4162−4163.
(24) Li, Z. D.; Zhou, Y.; Zhang, J. Y.; Tu, W. G.; Liu, Q.; Yu, T.; Zou, Z. G. *Cryst.Growth Des.* **2012**, *12*, 1476−1481.
(25) Chen, J. J.; Lu, L. Y.; Wang, W. Y. *J. Phys. Chem. C* **2012**, *116*, 10841−10847.
(26) Cun, W.; Wang, X. M.; Zhao, J. C.; Mai, B. X.; Sheng, G. Y.; Peng, P. A.; Fu, J. M. *J. Mater. Sci.* **2002**, *37*, 2989−2996.
(27) Fu, G.; Chen, H.; Chen, Z.; Zhang, J.; Kohler, H. *Sens. Actuators, B* **2002**, *81*, 308−312.
(28) Wang, Y. F.; Li, K. N.; Xu, Y. F.; Rao, H. S.; Su, C. Y.; Kuang, D. B. *Nanoscale* **2013**, *5*, 5940−5948.
(29) Wang, Y. F.; Li, K. N.; Xu, Y. F.; Su, C. Y.; Kuang, D. B. *Nano Energy* **2013**, *2*, 1287−1293.
(30) Li, Y. B.; Wang, Y. F.; Rao, H. S.; Wu, W. Q.; Li, K. N.; Su, C. Y.; Kuang, D. B. *ACS Appl. Mater. Interfaces* **2013**, *5*, 11865−11871.
(31) Yu, J. H.; Choi, G. M. *J. Electrochem. Soc.* **2001**, *148*, G307−G314.
(32) Rong, A.; Gao, X. P.; Li, G. R.; Yan, T. Y.; Zhu, H. Y.; Qu, J. Q.; Song, D. Y. *J. Phys. Chem. B* **2006**, *110*, 14754.
(33) Minami, T. *Semicond. Sci. Technol.* **2005**, *20*, S35−S44.
(34) Young, D. L.; Moutinho, H.; Yan, Y.; Coutts, T. J. *J. Appl. Phys.* **2002**, *92*, 310−319.
(35) Cheng, B. C.; Xiao, Y. H.; Wu, G. S.; Zhang, L. D. *Appl. Phys. Lett.* **2004**, *14*, 913−915.
(36) Cheng, B. C.; Xie, C. C.; Fang, L.; Xiao, Y. H.; Lei, S. J. *Mater. Chem. Phys.* **2011**, *129*, 713−717.
(37) Goldberger, J.; Sirbuly, D. J.; Law, M.; Yang, P. *J. Phys. Chem. B* **2005**, *109*, 9−14.
(38) Yu, P. Y.; Cardona, M. *Fundamentals of Semiconducotors: Physics and Materials Properties*; Springer: Berlin, 2001.
(39) Taur, Y.; Ning, T. H. *Fundamentals of Modern VLSI Devices*; Cambridge University Press: Cambridge, 1998.
(40) C. Johnson, A.; Cohn, A.; Kaspar, T.; Chambers, S. A.; Salley, G. M.; Gamelin, D. R. *Phys. Rev. B* **2011**, *84*, 125203.
(41) Fu, S. P.; Chen, T. T.; Chen, Y. F. *Semicond. Sci. Technol.* **2006**, *21*, 244−249.
(42) Arnaudov, B.; Paskova, T.; Paskov, P. P.; Magnusson, B.; Valcheva, E.; Monemar, B.; Lu, H.; Schaff, W. J.; Amano, H.; Akasaki, I. *Phys. Rev. B* **2004**, *69*, 115216.
(43) Donmez1, O.; Yilmaz, M.; Erol, A.; Ulug, B.; Arikan, M. C.; Ulug, A.; Ajagunna, A. O.; Iliopoulos, E.; Georgakilas, A. *Phys. Status Solidi B* **2011**, *248*, 1172−1175.
(44) Dingle, R. *Phys. Rev. Lett.* **1969**, *23*, 579−581.
(45) Tang, Y.; Zhao, D. X.; Zhang, J. Y.; Shen, D. Z. *Phys. B* **2010**, *405*, 4551−4555.
(46) Vanheusden, K.; Warren, W. L.; Seager, C. H.; Tallant, D. R.; Voigt, J. A.; Gnade, B. E. *J. Appl. Phys.* **1996**, *79*, 7983−7990.
(47) van Dijken, A.; Meulenkamp, E. A.; Vanmaekelbergh, D.; Meijerink, A. *J. Phys. Chem. B* **2000**, *104*, 1715−1723.
(48) Janotti, A.; Van deWalle, C. G. *Phys. Rev. B* **2007**, *76*, 165202.
(49) Lin, B. X.; Fu, Z. X.; Jia, Y. B. *Appl. Phys. Lett.* **2001**, *79*, 943−945.
(50) Xu, P. S.; Sun, Y. M.; Shi, C. S.; Xu, F. Q.; Pan, H. B. *Nucl. Instrum. Methods Phys. Res., Sect. B* **2003**, *199*, 286−290.
(51) Korsunska, N. O.; Borkovska, L. V.; Bulakh, B. M.; Khomenkova, L. Y.; Kushnirenko, V. I; Markevich, I. V. *J. Lumin.* **2003**, *102*, 733.
(52) Vidya, R.; Ravindran, P.; Fjellvag, H.; Svensson, B. G.; Monakhov, E.; Ganchenkova, M.; Nieminen, R. M. *Phys. Rev. B* **2011**, *83*, 045206.